JACS
JOURNAL OF THE AMERICAN CHEMICAL SOCIETY
Article
pubs.acs.org/JACS

Catalytic Mechanism of the Glycyl Radical Enzyme 4-Hydroxyphenylacetate Decarboxylase from Continuum Electrostatic and QC/MM Calculations

Mikolaj Feliks,[†] Berta M. Martins,[‡] and G. Matthias Ullmann*,[†]

[†]Computational Biochemistry, University of Bayreuth, Universitätsstrasse 30, BGI, 95447 Bayreuth, Germany

[‡]Structural Biology/Biochemistry − Radical Enzymes, Humboldt-Universität zu Berlin, Unter den Linden 6, 10099 Berlin, Germany

Supporting Information

ABSTRACT: Using continuum electrostatics and QC/MM calculations, we investigate the catalytic cycle of the glycyl radical enzyme 4-hydroxyphenylacetate decarboxylase, an enzyme involved in the fermentative production of *p*-cresol from tyrosine in clostridia. On the basis of our calculations, we propose a five-step mechanism for the reaction. In the first step, the substrate 4-hydroxyphenylacetate is activated by an unusual concerted abstraction of an electron and a proton. Namely, Cys503 radical abstracts an electron from the substrate and Glu637 abstracts a proton. Thus in total, a hydrogen atom is abstracted from the substrate. In the second step, the carboxylic group readily splits off from the phenoxy-acetate radical anion to give carbon dioxide. This decarboxylation step is coupled to a proton transfer from Glu637 back to the phenolic hydroxyl group which leads to a *p*-hydroxybenzyl radical. The remaining steps of the reaction involve a rotation of the Cys503 side chain followed by a proton transfer from Glu505 to Cys503 and a hydrogen atom transfer from Cys503 to the *p*-hydroxybenzyl radical to form *p*-cresol. The calculated mechanism agrees with experimental data suggesting that both Cys503 and Glu637 are essential for the catalytic function of 4-hydroxyphenylacetate decarboxylase and that the substrate requires a hydroxyl group in *para*-position to the acetate moiety.

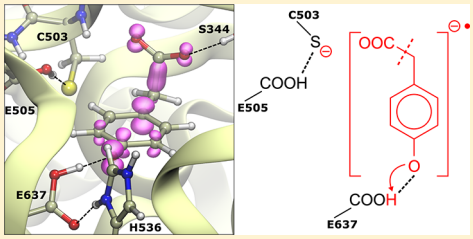

INTRODUCTION

In the last years, the number of known radical enzymes has greatly increased, and considerable advancements have been made in understanding the structure and function of these enzymes.[1−8] Radical enzymes use the high reactivity of radicals to challenge chemically difficult reactions. Some of them can be used in industry, opening new reaction paths which enable the conversion of otherwise nonreactive compounds.

In proteins, radicals can be localized on cofactors, like for example adenosylcobalamin (AdoCbl) or *S*-adenosylmethionine (SAM), or on amino acids (Gly, Tyr, Cys).[1,4] In most of the radical enzymes, the substrate is activated by abstraction of a hydrogen atom by transient radical species in the active site, such as a thiyl radical.[5] The activated substrate can undergo chemical reactions that would be impossible otherwise, for example, cleavage of a C−C bond.[5,6] In the course of the reaction, a product-related radical is generated, which is deactivated by accepting a hydrogen atom from the enzyme. Thus, deactivation of this product-related radical yields the product and regenerates the initial radical.

To date, six glycyl radical enzymes have been characterized: pyruvate-formate lyase, anaerobic ribonucleotide reductase, benzylsuccinate synthase, 4-hydroxyphenylacetate decarboxylase (4Hpad), B_{12}-independent glycerol dehydratase, and the recently discovered[11] choline TMA-lyase. Generally in these enzymes, a glycine residue is activated to a radical through abstraction of a hydrogen atom by the 5′-deoxyadenosyl radical of the corresponding SAM-dependent activating enzyme.[3,9,10] Upon substrate binding, the radical is transferred from the glycine to the active site cysteine, generating the thiyl radical which attacks the substrate.[10]

The enzyme 4Hpad,[12−14] which is the subject of this paper, catalyzes the formation of *p*-cresol from its substrate (Figure 1).

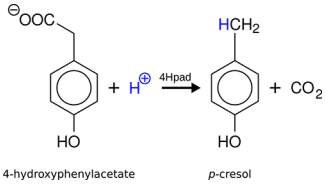

Figure 1. Microbial conversion of 4-hydroxyphenylacetate to *p*-cresol.

This reaction is part of the tyrosine fermentation in clostridia.[15] The product of the reaction is a virulence factor that is used by the bacterium against competitive organisms in the human intestine.[16] The 4Hpad activity has long been known in two strictly anaerobic bacteria, *Clostridium difficile* and *Clostridium scatologenes*.[12−15] However, its crystal structure has only been solved recently.[17]

Received: March 7, 2013
Published: September 12, 2013

   dx.doi.org/10.1021/ja402379q | *J. Am. Chem. Soc.* 2013, 135, 14574−14585

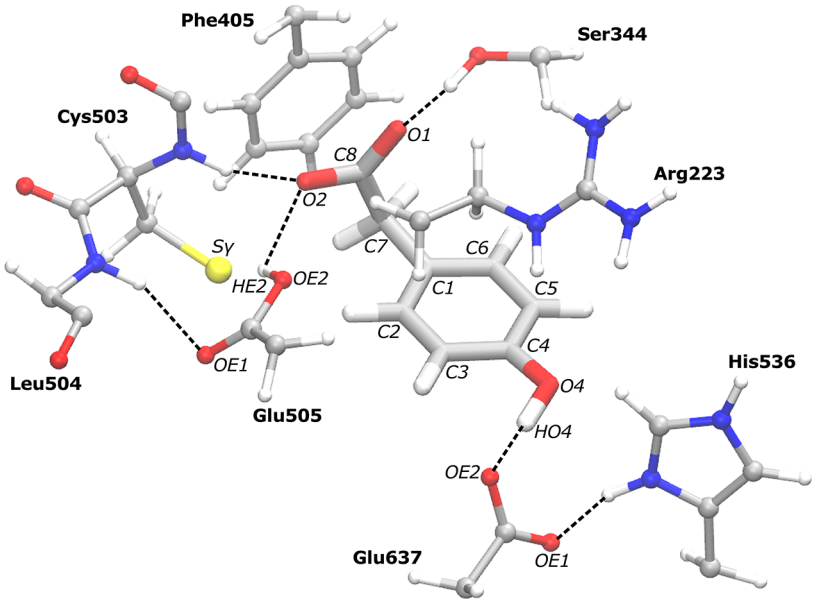

Figure 2. Close-up of the 4Hpad active site for the QC/MM-optimized geometry of the substate-bound state. The substrate is shown in a stick representation. The protein residues of the active site are shown in a ball-and-stick representation. The rest of the protein was omitted for clarity. Atoms discussed in the text are labeled.

A previously suggested reaction mechanism of 4Hpad assumed that 4-hydroxyphenylacetate binds in the active site with its hydroxyl group close to the radical cysteine Cys503.[12] This binding mode would allow Cys503 to initiate the reaction by abstraction of the phenolic hydrogen from the substrate generating a *p*-phenoxy-acetate radical anion that spontaneously decarboxylates. Contrary to expectations, the crystal structure shows a totally different binding mode of the substrate[17] (Figure 2). The hydroxyl group of the substrate is hydrogen bonded to Glu637, and the carboxylic group is located in the vicinity of Cys503 enabling a Kolbe-type decarboxylation.[18] However, the analysis of the crystal structure alone cannot provide a clear picture of the mechanism.

Theoretical calculations have provided many valuable insights into the intriguing chemistry of radical enzymes[19] as well as of enzymes catalyzing decarboxylations.[20−26] Pyruvate-formate lyase[27−31] and benzylsuccinate synthase[32] were the first glycyl radical enzymes to be studied computationally. General aspects of glycyl radical chemistry have also been addressed in the papers on the C−C bond cleavage[33] and the stability of protein radicals.[34,35] Quantum chemical calculations have recently been used to study the mechanism of the B_{12}-independent glycerol dehydratase, an enzyme with an active site that is similar to 4Hpad.[36−38]

In the present paper, we discuss a computational study on the catalytic mechanism of 4Hpad. The calculations were done on the high-resolution crystal structure of the substrate-bound form of the enzyme.[17] Two different computational methods have been employed. First, we performed electrostatic calculations combined with a Monte Carlo titration to study the protonation behavior of protonatable residues in the protein. The knowledge of protonation states is crucial for modeling the reaction mechanism.[39−41] Second, the reaction was modeled with a hybrid quantum chemical/molecular mechanical method (QC/MM).[42,43] The reaction mechanism was gradually constructed from potential energy surface (PES) scans followed by geometry optimizations. The reaction paths between the energetic minima were refined using the nudged elastic band (NEB) method.[44,45] Transition states were estimated as points of the highest energy on the NEB-calculated reaction profiles. Based on the QC/MM calculations, we propose a mechanism for the conversion of 4-hydroxyphenylacetate into *p*-cresol by 4Hpad that involves five elementary reaction steps.

METHODS

Preparation of the Continuum Electrostatic Model. The enzyme model was built from the X-ray structure of 4Hpad in complex with its substrate[17] (PDB code 2YAJ). The crystal structure shows Cys503 in two alternative conformations. We used the one, in which the S_γ atom is closer to the substrate as a starting point for our structure preparation. The physiologically active unit is a tetramer of heterodimers. Each heterodimer consists of a small subunit which binds two iron−sulfur clusters and a catalytic subunit which binds 4-hydroxyphenylacetate. Electrostatic calculations were done on the structure of the tetramer. For QC/MM calculations, only the catalytic subunit of the first monomer was used.

The starting model of the substrate state was setup in CHARMM.[46,47] Molecular mechanics parameters for the protein were taken from the CHARMM27 force field.[48] The parameters and atomic charges for 4-hydroxyphenylacetate were assigned by analogy to the compounds existing in the force field, namely tyrosine and glutamate. The atomic charges for iron−sulfur clusters were taken from the literature.[49]

In the next step, the protonation states of all titratable residues were set to their standard values at pH 7. The active site cysteine Cys503 as well as the carboxylic and the hydroxyl groups of the substrate were also treated as titratable sites. Missing hydrogen atoms were added by using the HBUILD routine of CHARMM. The positions of hydrogen atoms were subsequently geometry optimized with heavy atoms fixed to their initial positions. After optimization, the water molecules present in the crystal structure were removed from the model. In the continuum electrostatic model, these regions are filled with a high-dielectric medium. The protonation probabilities of titratable residues were evaluated on the basis of the Poisson−Boltzmann continuum electrostatic model combined with a Monte Carlo titration. The electrostatic calculations and the Monte Carlo titrations were carried out using MEAD[50] and GMCT,[51] respectively.

dx.doi.org/10.1021/ja402379q | J. Am. Chem. Soc. 2013, 135, 14574−14585

The Poisson−Boltzmann continuum electrostatic model was used with the following parameters. The interior of the protein was assigned a dielectric constant of $\varepsilon_p = 4$. The solvent was modeled as a medium with a dielectric constant of $\varepsilon_s = 80$, an ionic strength of $I = 100$ mM and a temperature of $T = 300$ K. The volume of the protein was defined by an ion exclusion layer of 2.0 Å and a solvent probe radius of 1.4 Å. The electrostatic potential was calculated on a grid of 121^3 nodes with four focusing steps at a resolution of 2.0, 1.0, 0.5, and 0.25 Å. The larger grid was geometrically centered at the molecule, while the finer grids were geometrically centered on the group of interest. The protonation probability of each titratable residue was calculated by a Metropolis Monte Carlo algorithm as a function of pH. The pH was varied from 0 to 14 in steps of 0.2 pH units. For every pH step, the MC calculation consisted of 100 equilibration scans and 3000 production scans at $T = 300$ *K*.

QC/MM Model Setup. The QC/MM models were setup on the basis of the catalytic subunit of the first monomer of the crystal structure. The rest of the protein was not included. Hydrogen atoms were now added according to the previous electrostatic calculations. The radical was introduced to the model by deletion of the H_γ hydrogen of Cys503. The charge of the removed hydrogen atom was added to the charge of the remaining S_γ atom. In the next step, the positions of hydrogen atoms were geometry optimized in CHARMM. Unlike for the continuum electrostatic model, all water molecules present in the crystal structure were preserved. The complete CHARMM-prepared MM model of the catalytic domain consisted of 869 residues, 1009 water molecules, and one 4-hydroxyphenylacetate molecule (16 547 atoms in total).

Further structure preparations and QC/MM calculations were performed by Python scripts written within the framework of the pDynamo software library,[52] version 1.7.2. The quantum chemical part of calculations was handled by the pDynamo-coupled program ORCA.[53] The B3LYP[54−57] density functional theory method and the CHARMM27 force field were employed as QC and MM potentials, respectively. The B3LYP functional has a well-documented history of use in studies on radical enzymes.[19] All QC/MM calculations, including geometry optimizations, were performed with electrostatic embedding, which incorporates MM charges into the QC wave function. To saturate the valence at the QC/MM boundary, link atoms as implemented in the pDynamo library were introduced. A medium-sized 6-31G(d) basis set was used for the geometry optimizations. Final energies and atomic properties (Mulliken spin densities) were evaluated by performing single-point energy calculations with the 6-311++G(2d,2p) basis set on the previously optimized geometries. Four QC/MM models that varied in the size of the QC part were prepared. The minimal model (M1) includes in the QC part only the substrate and the side chains of Cys503, Glu505 and Glu637. The M2 model extends the QC region of the M1 model with the Ser344 side chain. This model is further extended by inclusion of the His536 side chain into the QC part (M3). The largest model (M4) incorporates into the QC region also a fragment of the protein backbone that is adjacent to Cys503. The charge of the QC region was −2 for the models M1 and M2 and −1 for the models M3 and M4. The multiplicity of all models was 2.

Since the active site of 4Hpad is buried inside the protein, no solvent water molecules in addition to those present in the crystal structure were added to the models. The external parts of the model were kept restrained during the geometry optimizations. Harmonic restraints were applied for MM atoms at the distance ≥8 Å away from any QC atom. That is, every QC atom was surrounded by an 8 Å sphere of fully movable atoms. At the distance between 8 and 16 Å from every QC atom the force constants for restraints were set to linearly increase from 0 to 12 kcal/mol. Outside the distance of 16 Å the restraints were set to the maximum force constant of 12 kcal/mol. For model M1, 841 atoms were unrestrained, and the remaining 15 706 atoms were restrained (out of which 12 653 atoms with the maximum force constant). For the largest model M4, 1176 atoms were allowed to move freely, and 15 371 atoms were kept restrained (11 27 with the maximum force constant).

Reaction Path Search. The initial exploration of the reaction path was performed for the M1 model. The geometry of the substrate state was calculated by simply optimizing the CHARMM-prepared structure. In the first step, the structure was preoptimized only with the force field. In the second step, the geometry obtained from MM optimizations was optimized with the QC/MM potential. The MM optimization was performed only once for the substrate state, and all further optimizations were done using the QC/MM potential. Throughout the calculations, external parts of the QC/MM model were kept restrained according to the aforementioned scheme. A conjugate gradients algorithm was used in both MM and QC/MM optimizations with the convergence criterion of the root-mean-square gradient of the energy <0.01 kcal/mol Å.

Starting from the substrate geometry, the reaction path was progressively explored by performing PES scans followed by geometry optimizations. The PES scans were done by extending or shortening selected distances between two atoms, usually in steps of ±0.1 Å. The distance was assumed to be the major component of the reaction coordinate. For example, to investigate the decarboxylation step by a PES scan, the distance between atoms C7 and C8 of the substrate was extended. At each point of the scan a constrained geometry optimization was performed. A scan usually generated 5−20 structures that approximated the path of the particular reaction step. The structure of the highest energy along the selected reaction coordinate can be treated as the first approximation of the transition-state geometry. The last structure from the scan was optimized to find the geometry of a new intermediate. This geometry was subsequently used to initiate another scan to find the consecutive intermediate on the reaction path. A PES scan in the reverse direction was also performed to check whether the starting structure can be regenerated; if so, the selected reaction coordinate was assumed to correctly represent the actual one.

Since the reaction coordinate for a PES scan is always selected with a certain bias, the exact reaction paths between the calculated minima were determined by using the modified NEB method[44,45] from the pDynamo library. This method works by generating a series of interpolated frames between the previously calculated geometries of the two energy minima. The frames are subsequently linked with a merit function and optimized together to find the actual minimum energy path (MEP). A MEP was usually calculated for 10−14 frames. On top of the NEB-derived reaction paths, single-point energy evaluations with the larger basis set were performed to calculate the final reaction profiles. Transition-state geometries were assumed to be the points of the highest energy on the NEB-generated reaction profiles.

Reaction paths for the models with a larger QC region were calculated starting from the optimized minima of the M1 model. The unrestrained parts of the M1 model were cut from the optimized geometries and embedded into the initial geometries of models M2−M4. In the next step, the so-prepared geometries were reoptimized. NEB calculations and single-point energy evaluations were performed anew from these optimized geometries. To validate this approach, the mechanism for the M2 model was additionally studied by systematic exploration of the PES as described before. Regardless of the used approach, the resulting geometries and energetics are very similar. For example, the substrate state of the M2 model optimized starting from the M1 model is only 0.04 kcal/mol different in energy than the one optimized anew. The root-mean-square deviation (RMSD) was calculated to be <0.01 Å between the two geometries taking all atoms into the calculation of the RMSD. Thus, in both cases the model converges to the same minimum. Similar observations were made for the other intermediates.

RESULTS AND DISCUSSIONS

Protonation States of Active Site Residues. The active site of 4Hpad shows several protonatable residues (see Figure 2). Glu505 is located within the loop containing the radical cysteine and is in hydrogen-bond distance from both Cys503 and the carboxylic group of 4-hydroxyphenylacetate. Glu637 is

dx.doi.org/10.1021/ja402379q | J. Am. Chem. Soc. 2013, 135, 14574−14585

positioned on the opposite end of the active site and coordinates the hydroxyl group of the substrate by a hydrogen bond. His536 interacts closely with Glu637 and also with the hydroxyl group of the substrate. We performed electrostatic calculations on the substrate-bound form of the enzyme to determine the protonation behavior. In the lowest energy protonation state at pH = 7 (Table 1), Glu505 is protonated,

Table 1. Lowest Energy Protonation States of the Active Site[a]

state	ΔE (kcal/mol)	Glu505	His536	Glu637	substrate
1	0.0	0	ε, δ(+)	(−)	−OH, −COO(−)
2	1.8	0	ε	0	−OH, −COO(−)
3	2.1	0	δ	0	−OH, −COO(−)
4	5.3	0	ε, δ(+)	0	−OH, −COO(−)
5	5.6	0	ε, δ(+)	(−)	−OH, −COOH
6	8.3	0	ε	0	−OH, −COOH
7	8.6	(−)	δ	0	−OH, −COOH
8	8.6	(−)	ε	0	−OH, −COOH
9	8.6	(−)	ε, δ(+)	(−)	−OH, −COOH
10	8.6	0	δ	(−)	−OH, −COO(−)
11	9.0	0	δ	0	−OH, −COOH
12	10.4	0	δ	(−)	−OH, −COOH
13	11.7	(−)	ε, δ(+)	0	−OH, −COOH
14	11.7	(−)	ε, δ(+)	0	−OH, −COO(−)
15	12.3	(−)	δ	0	−OH, −COO(−)
16	12.7	(−)	ε	0	−OH, −COO(−)
17	13.7	(−)	ε, δ(+)	(−)	−OH, −COO(−)
18	16.0	0	ε, δ(+)	0	−OH, −COOH
19	16.5	0	ε	(−)	−OH, −COO(−)
20	16.6	0	ε, δ(+)	0	−O(−), −COOH

[a]The protonation states were determined from the electrostatic calculations performed on the complete tetramer of the substrate-bound form of 4Hpad.

Glu637 is deprotonated, and His536 is in its imidazolium form, i.e., positively charged. The positive charge on His536 is stabilized by the negatively charged Glu637. The calculations predict that the substrate binds in the active site with its carboxylic group deprotonated and its hydroxyl group protonated. The negative charge of the former is stabilized by a network of hydrogen bonds from Ser344, Glu505 (which is protonated), and a part of the protein backbone near Cys503. The total charge of the active site as depicted in Figure 2 is zero.

Selection of a QC/MM Model. An ideal QC/MM model would include the substrate and its complete surrounding in the QC part. As often in calculations involving quantum chemistry, limited computer resources impose some restrictions on the size of the QC part that can be effectively handled. Therefore, the reaction was first studied with the M1 model whose QC part was limited to 35 atoms (38 with link atoms). The minimal QC part includes the substrate and the side chains of Cys503, Glu505 and Glu637. Only the reacting parts of the system are treated at the QC level, and the nonreactive ones are treated at the MM level. Clearly, the latter can also be involved in the catalysis in one way or another by intermolecular interactions with the reacting region.

Although the nonreactive parts of the enzyme are "visible" by electrostatic embedding, it is useful to recalculate the reaction path with models with an extend QC region, because the description of interactions by point charges may not always be accurate enough. In addition to M1, three models that differed in the size of the QC region were also prepared. The M2 model extends the QC part by addition of the Ser344 side chain (40 atoms; 44 with link-atoms). Ser344 forms a hydrogen bond to the carboxylic group of the substrate that may have some influence on the energetics of the decarboxylation step. The M3 model further extends the M2 model with His536 (55 atoms; 65 with link-atoms). This residue is hydrogen-bonded to Glu637, which is also hydrogen-bonded to the substrate. The positive charge on His536 can stabilize the deprotonated form of Glu637 in the substrate-bound state. Moreover, the HD1 atom of His536 is only 2.7 Å away from the O4 atom of the substrate (geometry of the crystal structure with CHARMM-optimized hydrogen atoms). This arrangement suggests that His536 may stabilize also a negative charge on reaction intermediates during the catalytic cycle. The second positively charged residue in the vicinity of the active site is Arg223. However, this residue points away from the substrate and forms hydrogen bonds to the parts of the protein backbone at Ile219, Gln221, and Gly532. Thus, Arg223 seems to play a structural role and was therefore only treated at the MM level. The last model M4 incorporates in the QC region also a fragment of the protein backbone at Cys503 (66 atoms; 73 with link-atoms). This backbone fragment forms hydrogen bonds to the carboxylic group of the substrate and to the carboxylic group of Glu505.

Calculated Reaction Mechanism. Unless mentioned otherwise, the geometries and energies discussed in this section are of the largest QC/MM model (M4). The overall calculated reaction path involves five steps (see Figure 3 for a schematic picture and Table 2 for reaction energetics). First, the substrate is activated by a simultaneous electron and proton transfer forming a phenoxy-acetate radical anion (Sub→In1). Second, the phenoxy-acetate radical anion undergoes decarboxylation forming a *p*-hydroxybenzyl radical (In1→In2). Next, the Cys503 side chain rotates toward the methylene radical group (In2→In2′). This step is followed by the proton transfer between Glu505 and Cys503 (In2′→In3). During the last reaction step, *p*-cresol is generated by transferring a hydrogen from Cys503 to the product-related radical intermediate (In3→Pro). The reaction mechanism, which was proposed before the structure was known,[12] is unlikely since the substrate would have to bind in a different binding mode (basically 180° rotated) resulting in unfavorable interactions with the protein (Supporting Information, SI). The mechanism described here is consistent with experimental data.

Substrate State. The initial QC/MM optimization introduces small geometrical changes into the CHARMM-prepared structure. Since the crystal structure lacks a radical in the active site, these changes most likely result from introducing the radical into the model. In the starting structure, the proton bound to the carboxyl group of Glu505 is 2.1 Å away from the S_γ atom of Cys503 (see Figure 2 for atom names) which indicates a hydrogen bond between Glu505 and Cys503. However, this putative hydrogen bond breaks after the optimization, and another hydrogen bond is created between the carboxylic group of Glu505 and the carboxylic group of the substrate. In model M4, the distance between the proton of the carboxyl group of Glu505 to the closest carboxylic oxygen atom of the substrate is 1.9 Å. For the models that do not include the backbone fragment at Cys503 in the QC part, this distance increases to about 2.3 Å.

dx.doi.org/10.1021/ja402379q | J. Am. Chem. Soc. 2013, 135, 14574−14585

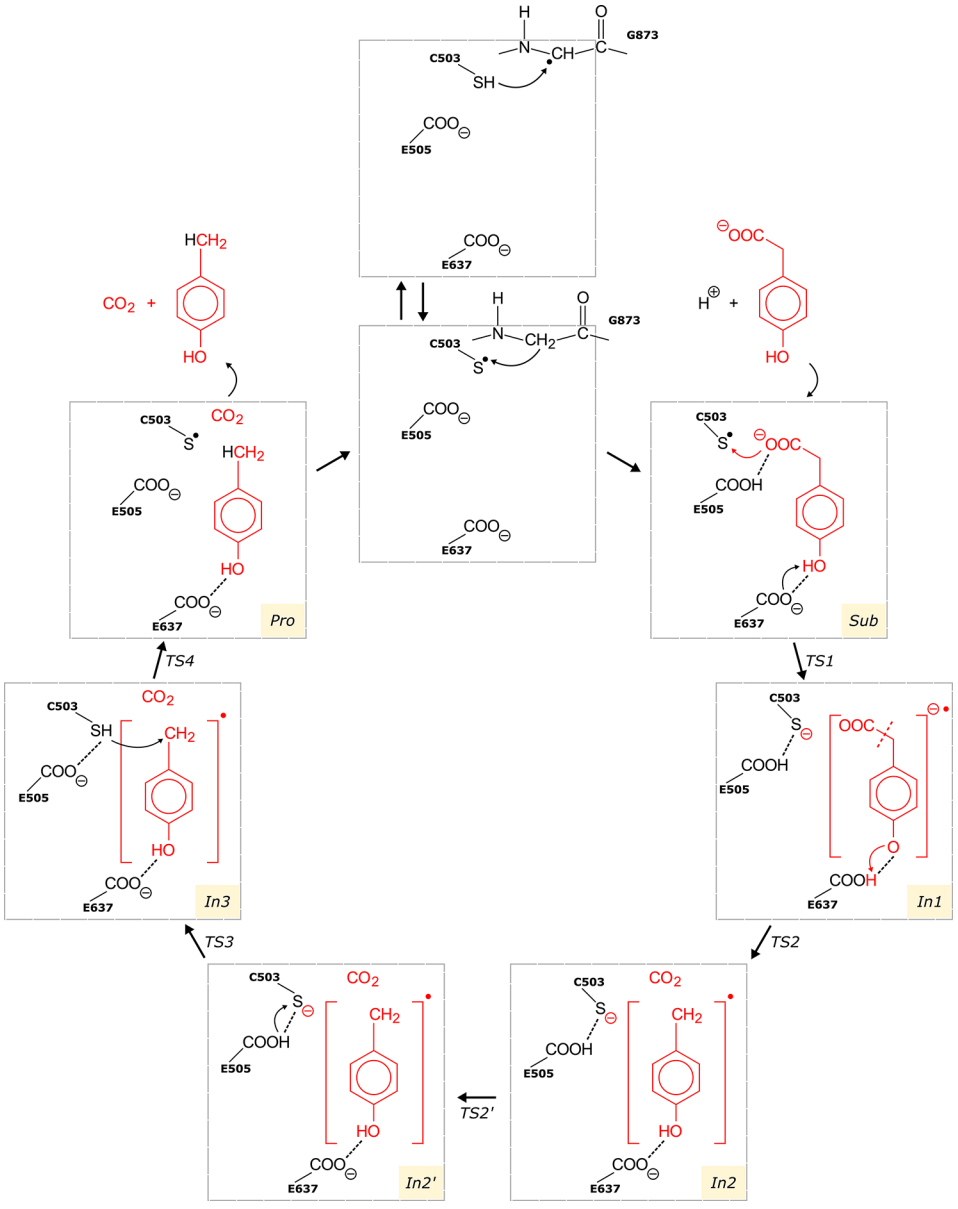

Figure 3. Catalytic mechanism of 4Hpad. The chemical conversion steps of the substrate to the product are derived from the calculations.

Table 2. Summary of the Reaction Energetics (kcal/mol) Calculated for Different QC/MM Models[a]

	Sub→In1		In1→In2		In2→In2′		In2′→In3		In3→Pro	
	$\Delta E^{\ddagger}$	ΔE	$\Delta E^{\ddagger}$	ΔE	$\Delta E^{\ddagger}$	ΔE	$\Delta E^{\ddagger}$	ΔE	$\Delta E^{\ddagger}$	ΔE
M1	1.9	−0.8	4.2	2.3	4.0	2.6	3.4	0.1	7.1	−3.1
$M1_{small}$	0.4	−4.5	4.6	3.8	4.8	2.5	4.3	2.8	7.3	−5.0
M2	1.5	−1.2	7.1	4.2	4.1	2.4	3.3	0.3	7.2	−3.2
$M2_{small}$	0.6	−4.3	8.8	7.9	4.8	2.1	4.8	3.0	7.2	−5.1
M3	1.2	−0.4	6.4	3.4	4.2	2.3	3.6	0.6	6.3	−3.3
$M3_{small}$	1.1	−1.7	6.9	5.5	4.8	1.9	4.4	3.2	7.0	−5.5
M4	1.0	−1.8	6.9	3.6	4.9	4.2	5.4	−0.7	6.1	−2.4
$M4_{small}$	1.9	−0.6	8.2	6.6	4.4	3.2	5.0	−0.2	5.1	−4.7

[a]The energies calculated with the smaller 6-31G(d) basis set are in the rows marked with small. The other energies were calculated with the larger 6-311++G(2d,2p) basis set. $\Delta E^{\ddagger}$ and ΔE are the activation energy and reaction energy of the particular reaction step, respectively.

For models M1−M3, the calculated geometry of the substrate state is very similar. The M4 model shows a slightly shorter hydrogen bond between the O2 atom of the substrate and the backbone hydrogen atom at Cys503. Also the aforementioned HE2···O2 hydrogen bond is shorter in the M4 model, which can be related to the inclusion of the backbone fragment into the QC region. Nonetheless, the

dx.doi.org/10.1021/ja402379q | J. Am. Chem. Soc. 2013, 135, 14574−14585

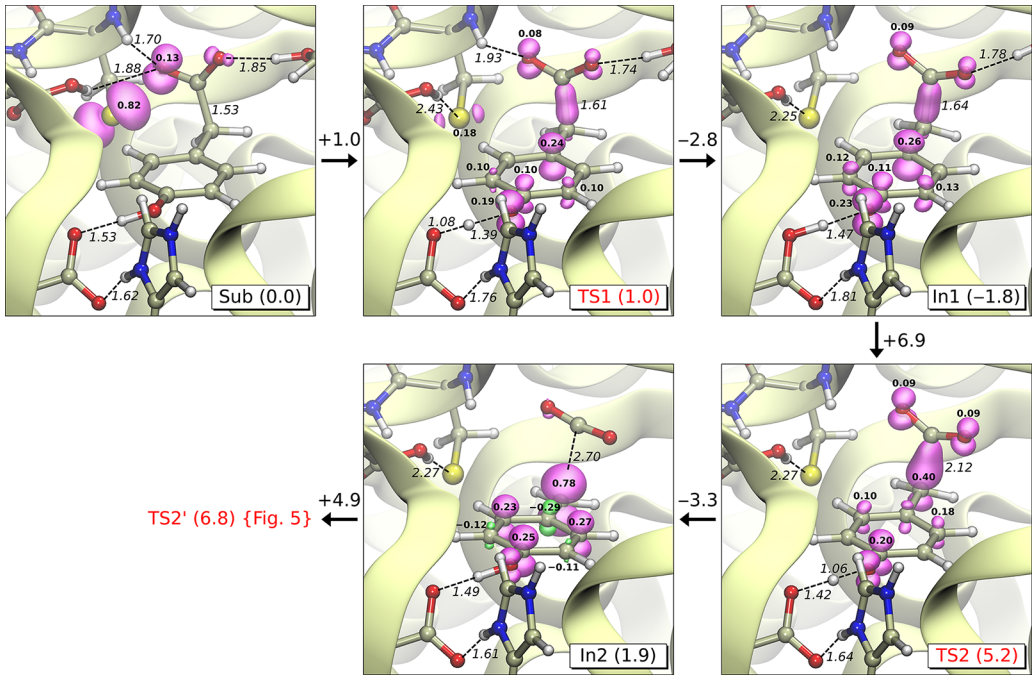

Figure 4. QC/MM-optimized geometries of intermediates and transition states for the activation and decarboxylation of the substrate (model M4). The transition states are the highest energy points on the NEB-calculated reaction profiles (see Figure 6). The energies are given in kcal/mol with respect to the substrate state (Sub). Numbers at the arrows indicate changes of the energy. Numbers in italics are distances relevant for the current reaction step (in Å). Mulliken atomic spin densities are depicted in bold numbers (for clarity, only the ones of the absolute value ≥0.1). The 3D spin density (magenta, positive; green, negative) is shown at the isovalue of 0.01 au. The model was visualized in VMD.[59]

RMSD between the four models of the substrate state is always <0.03 Å.

The substrate state shows the radical located mostly on the S_γ atom of Cys503. The Mulliken spin density for this atom was calculated to be 0.82 (Figure 4). Thiyl radicals are known to lack any kind of radical delocalization.[33] Interestingly, a large part of the remaining spin density (0.13) resides on the O2 atom of the carboxylic group of the substrate. For the models that do not include Ser344 or the backbone fragment at Cys503 in the QC part, the spin distribution is slightly different. In model M1, the Mulliken spin density calculated on the S_γ atom is 0.69, and the spin on the O2 atom is 0.25. The shortest contact between the thiyl radical and the substrate is the S_γ···O2 distance. In the crystal structure, the S_γ and O2 atoms are 3.3 Å away from each other. This distance decreases to 2.7 Å after the QC/MM optimization. The carboxylic group of the substrate is negatively charged and so is the center of the radical at Cys503. However, the hydrogen bonds provided by the active site residues in particular from Glu505 and from the protein backbone keep Cys503 and the substrate relatively close to each other. As will be discussed later, close contact between the radical center at Cys503 and the carboxylic group of the substrate is crucial for the electron transfer between these two which activates the latter.

Radical Transfer from Cys503 to the Substrate (Step I). The catalytic cycle in most of the radical enzymes is thought to start by the removal of a hydrogen atom from the substrate.[5] This activation is usually accomplished by the homolytic cleavage of a nonreactive C−H bond. The activated substrate-derived radical intermediate enters a series of reactions, during which it is converted into a product-related radical intermediate. The final product is formed by the transfer of a hydrogen atom from the enzyme.

The binding mode of 4-hydroxyphenylacetate in the active site of 4Hpad suggests that the radical transfer occurs between the radical center at Cys503 and the carboxylic group of the substrate. Since the electrostatic calculations indicate that the substrate binds to the enzyme with its carboxylic group deprotonated, Cys503 may not abstract a hydrogen atom from the substrate. On the other hand, the optimized geometry of the substrate state shows that the S_γ atom of Cys503 and the O2 atom of 4-hydroxyphenylacetate are in close proximity (Figure 4). If the C7−C8 bond of the substrate is extended by performing a PES scan along this bond, the system readily arrives at the first intermediate (In1) which is a phenoxy-acetate radical anion. In this first intermediate, the C7−C8 bond is extended by <0.2 Å compared to the substrate geometry.

The optimized geometry of the first intermediate state shows several interesting features. First, the radical has left Cys503 and is now delocalized over the aromatic ring (see In1 on Figure 4). The observed odd-alternant spin pattern is similar to that of tyrosyl radicals.[33] Most of the spin density is shared between the atoms C1 and O4 of the phenoxy-acetate radical anion intermediate (0.26 and 0.23, respectively) as well as C3, C4, and C5 (0.12 equally). Second, the proton of the hydroxyl group of the substrate (HO4) is now transferred to the carboxylic group of Glu637. Thus, the substrate is activated by a concerted abstraction of an electron and a proton, i.e., *de facto* a hydrogen atom. The key difference with respect to other radical enzymes is that in 4Hpad the electron and the proton are abstracted from the substrate separately at the opposite ends of the active site. Thus, the simultaneous participation of two active site residues, namely Cys503 and Glu637, is required for this step.

The geometry of the first intermediate state also shows that the hydrogen bond from Glu505 to the carboxylic group of the substrate has broken and that a new hydrogen bond has formed

dx.doi.org/10.1021/ja402379q | J. Am. Chem. Soc. 2013, 135, 14574−14585

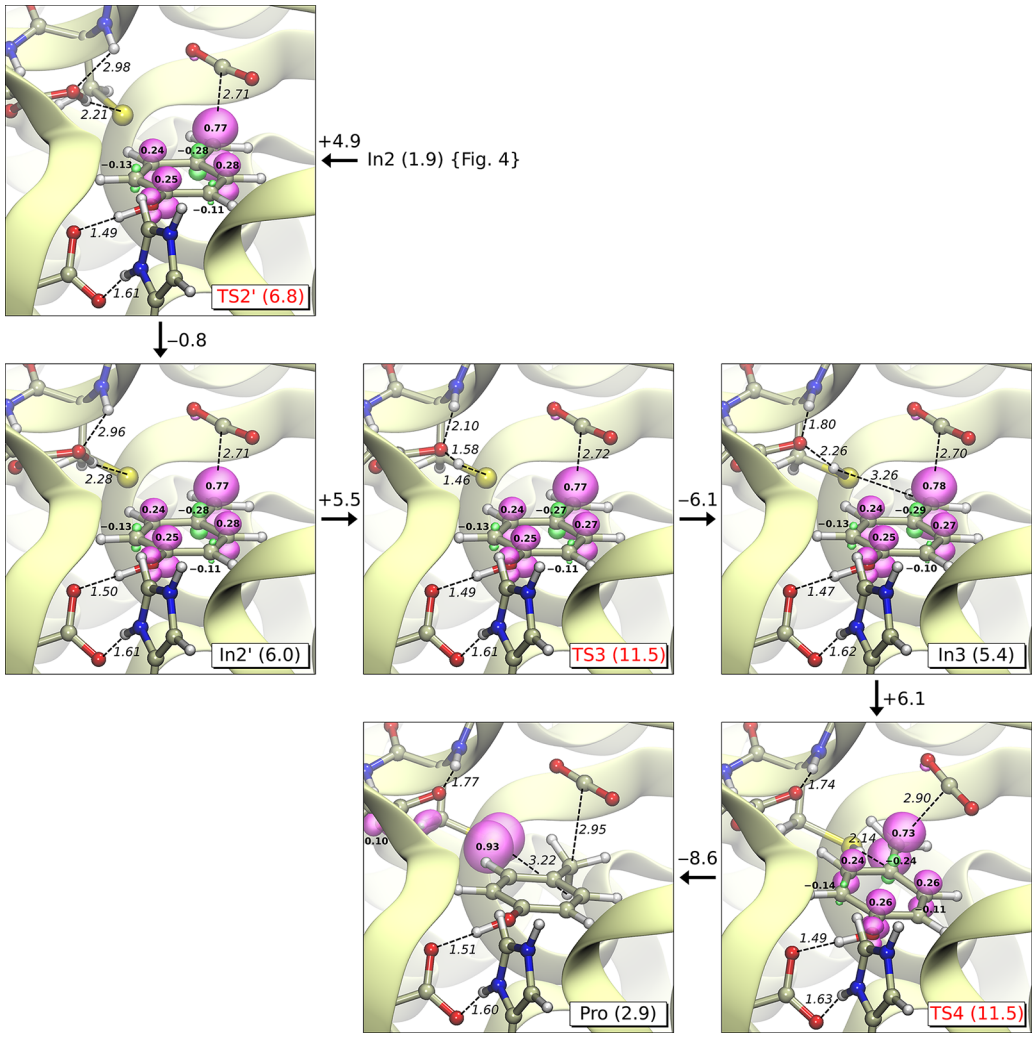

Figure 5. QC/MM-optimized geometries of intermediates and transition states for step III (rotation of the Cys503 side chain), IV (proton transfer Glu505→Cys503), and V (radical back-transfer methylene group intermediate→Cys503). See description under Figure 4 for details.

between Glu505 and Cys503 (Figure 5). The proton bound to the carboxylic group of Glu505 is now as close as 2.3 Å from the S_γ atom of Cys503. This structural change is related to the fact that a negative charge is localized on the S_γ atom after the radical transfer from Cys503 to the substrate. Also the carboxylic group of the substrate moves toward the side chain of Ser344, which in turn slightly changes its conformation. This movement does not affect the hydrogen-bond length between these groups. The phenoxy-acetate radical anion remains negatively charged because the hydroxyl proton has moved to Glu637. From the analysis of Mulliken charges, it can be seen that the charge distribution on the carboxylic and the hydroxyl groups of the reaction intermediate does not change significantly after the first reaction step. The differences in charge distribution are most obvious for the aromatic ring and for the S_γ atom of Cys503, which becomes considerably more negatively charged (the Mulliken charge on this atom changes from −0.17 to −0.80).

To explore the energetics of the activation step in detail, a reaction path between the substrate and the first intermediate states was calculated by using the NEB method. Eleven frames were used for the calculation of the path. The barrier for the substrate activation in model M4 was calculated to be as low as 1.0 kcal/mol (see Sub→In1 in Table 2). The other models predict somewhat higher barriers; about 1.5 kcal/mol for models M1 or M2 and 1.2 kcal/mol for model M3. All models give nearly the same geometry of In1. The intermediate state was calculated to be −1.8 kcal/mol more stable than the substrate state (M4). The predicted energetics varies slightly depending on the QC/MM model used. For the minimal model M1, the first intermediate was calculated to be only −0.8 kcal/mol more stable than the substrate state. After Ser344 has been included in the QC region, In1 becomes −1.2 kcal/mol lower in energy than Sub (M2). The inclusion of both Ser344 and His536 into the QC part gives the energy of In1 only −0.4 kcal/mol lower with respect to the substrate state (M3). These results suggest that the presence of His536 in the QC region helps to stabilize the negative charge on Glu637 in the substrate state.

Decarboxylation of the Substrate-Derived Intermediate (Step II). After removal of an electron and the phenolic proton, the phenoxy-acetate radical anion (activated substrate) can undergo decarboxylation. During this reaction step a *p*-hydroxybenzyl radical, which is the product-related intermediate (In2 in Figure 4), will be generated. To study the release of the carboxylic group, a PES was performed along the C7−C8 bond. The bond was extended in steps of 0.1 Å. Next, the actual reaction path was recalculated with the NEB method.

dx.doi.org/10.1021/ja402379q | J. Am. Chem. Soc. 2013, 135, 14574−14585

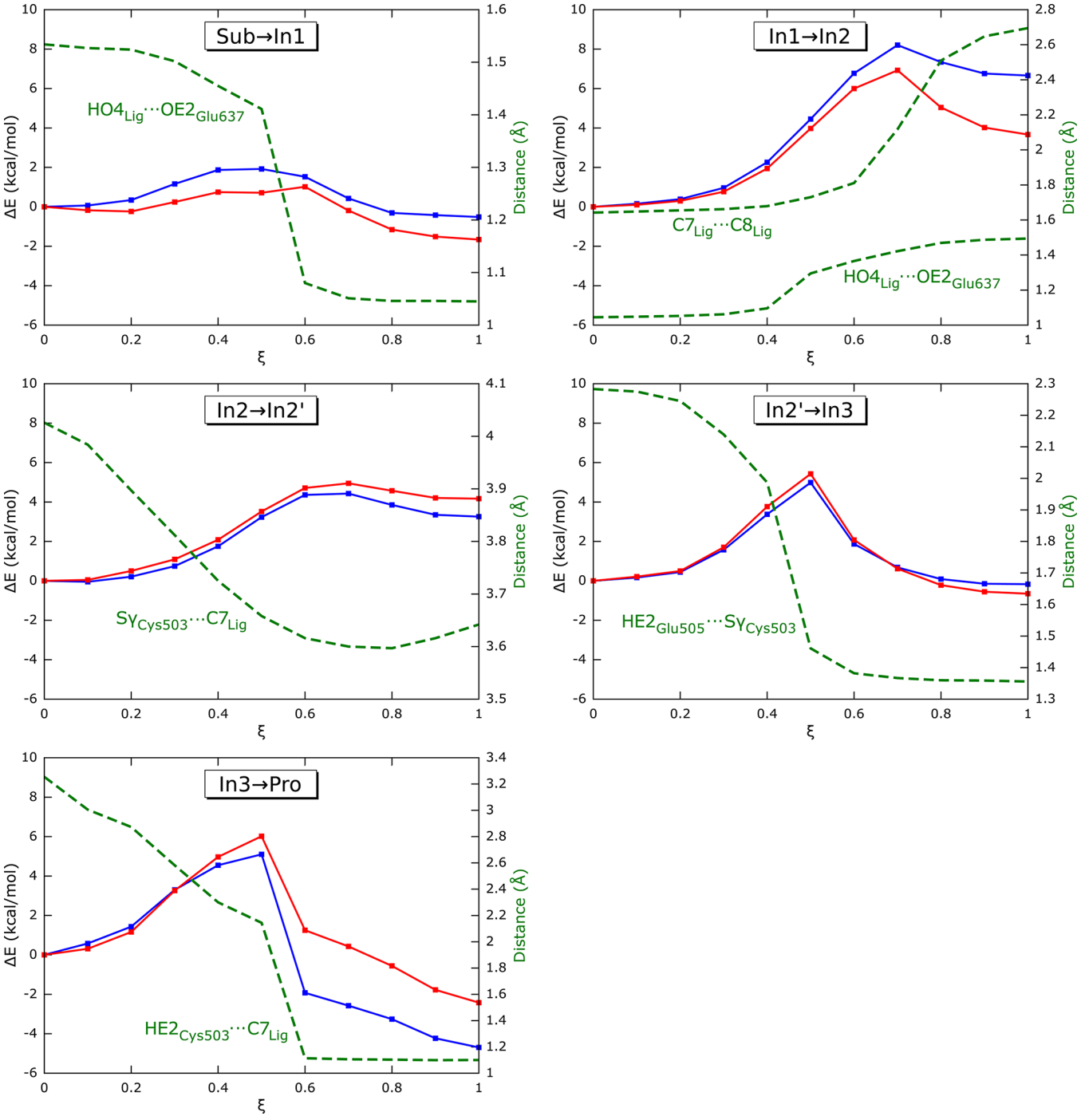

Figure 6. NEB-derived reaction profiles for the five reaction steps (model M4). Blue and red lines represent the profiles calculated with the smaller 6-31G(d) and the larger 6-311++G(2d,2p) basis set, respectively. ξ is the normalized reaction coordinate ($\xi = 0$ for substrate state; $\xi = 1$ for product state). Changes of key intra- or intermolecular distances are shown on the second *Y*-axis.

The decarboxylation was found to be coupled with a proton transfer from Glu637 back to the reaction intermediate. From the NEB-calculated reaction path, it can be seen that the actual proton transfer and the cleavage of the carbon−carbon bond occur at the same point on the reaction coordinate (see In1→In2 on Figure 6). The C7−C8 bond of the acetate moiety becomes weak after one electron is lost from the substrate. The addition of a proton from Glu637 shifts the remaining electron density toward the aromatic ring, which facilitates the decarboxylation. After the release of carbon dioxide, the radical moves from the aromatic ring to the atom C7. The Mulliken spin density on C7 is now calculated to be 0.78. The remaining spin density is localized at the aromatic ring showing an odd-alternant spin pattern. The final C7···C8 distance for dissociated CO_2 is 2.7 Å. The calculated geometry of In2 for all QC/MM models is again very similar. During the C7−C8 bond extension, the hydrogen bond between the carboxylic group of the intermediate and Ser344 breaks. Another hydrogen bond is created between Ser344 and the carbonyl oxygen atom of the protein backbone at Asn403. From this reaction step on, Ser344 points away from the active site.

dx.doi.org/10.1021/ja402379q | J. Am. Chem. Soc. 2013, 135, 14574−14585

The lowest barrier for the decarboxylation of 4.2 kcal/mol was calculated for the M1 model (see In1→In2 in Table 2). Model M2 which includes Ser344 in the QC region gives a somewhat higher barrier of 7.1 kcal/mol. Ser344 in the QC region seems to interact more strongly with the leaving carboxylic group, which elevates the barrier. However, model M3 which includes in addition His536 in the QC region, the effect of Ser344 partly canceled, and the barrier is lowered to 6.4 kcal/mol. The barrier is again slightly elevated to 6.9 kcal/mol in the M4 model, because the leaving carboxylic group has to overcome additional stabilizing interactions from the part of the protein backbone at Cys503, which is now included in the QC region.

Rotation of the Cys503 Side Chain (Step III). To complete the reaction, the *p*-hydroxybenzyl radical is assumed to abstract a hydrogen atom from the enzyme. Clearly, the only proton accessible to the methylene group is the one at the carboxylic group of Glu505 (HE2). As mentioned before, during the activation step a hydrogen bond is created between Glu505 and the negatively charged Cys503. In In2, the proton bound to the carboxylic group of Glu505 is 2.3 Å away from the S_γ atom of Cys503. This short contact suggests a possibility for a proton transfer from Glu505 to Cys503. However, a PES performed along the HE2···S_γ distance shows that such a proton transfer is not easily feasible, and the energy minimum corresponding to the protonated Cys503 cannot be found. From the scan, one can conclude that the proton is considerably more stable at Glu505 than at Cys503. The same observation was made starting the scan either from In1 or In2. Another option is that Glu505 delivers its carboxylic proton directly to the *p*-hydroxybenzyl radical intermediate, and the electron comes from Cys503. This scenario would resemble the coupled electron and proton transfer that occurs during the activation of the substrate. A PES performed along the HE2···C7 distance precludes, however, the possibility that the proton and electron come separately. The energy of this scan was found to be increasing to more than 20 kcal/mol, and a product state could not be localized, which can be explained by the too long HE2···C7 distance (of about 4.3 Å) and the unfavorable orientation of the methylene group toward Cys503.

However, the side chain of Cys503 can easily rotate toward the reaction intermediate (see TS2′ and In2′ on Figure 5). The barrier for this rotation was found to be as low as 4.9 kcal/mol (M4). For the models that do not include the Cys503 backbone fragment in the QC region, the barrier was calculated to be 4.0−4.2 kcal/mol. The resulting conformational intermediate In2′ is 4.2 kcal/mol higher in energy than In2 (2.6, 2.4, and 2.3 kcal/mol for models M1−M3, respectively). Regardless of the QC/MM model used, the optimized geometry of In2′ remains almost the same. Geometrically, the rotation involves a slight change in the conformation of the protein backbone between Cys503 and Glu505. This conformational change is supported by the crystal structure of 4Hpad, which shows the side chain of Cys503 in two alternative conformations.[17] Two hydrogen bonds between Glu505 and the backbone fragment become shorter, namely the OE1···H_{Cys503} bond (from 3.2 to 3.0 Å) and the OE2···H_{Leu504} bond (from 2.6 to 1.9 Å). The hydrogen bond length between the HE2 atom of Glu505 and the S_γ atom of Cys503 does not change during the rotation.

Proton Transfer from Glu505 to Cys503 (Step IV). After the rotation of the Cys503 side chain, the proton transfer between Glu505 and Cys503 becomes feasible. The modified hydrogen bonds between the protein backbone and Glu505 can now better stabilize the negative charge that will be localized on the carboxylic group of Glu505 after the deprotonation of this residue. The proton transfer was initially modeled by a PES scan performed along the HE2···S_γ distance and subsequently recalculated by using the NEB method. The barrier was calculated to be about 3.5 kcal/mol for the smaller QC/MM models and 5.4 kcal/mol for the M4 model (see In2′→In3 in Table 2). The transition state taken from the NEB-profile shows the HE2 proton located in between the OE2 atom of Glu505 and the S_γ atom of Cys503. Transfer of the proton to Cys503 in the M4 model gives the intermediate In3 that is energetically lower by only −0.7 kcal/mol with respect to In2′. For the M1 model, In3 has practically the same energy as In2′ and becomes slightly less stable for the models M2 and M3 (0.3 and 0.6 kcal/mol, respectively; Figure 7). In general, step IV

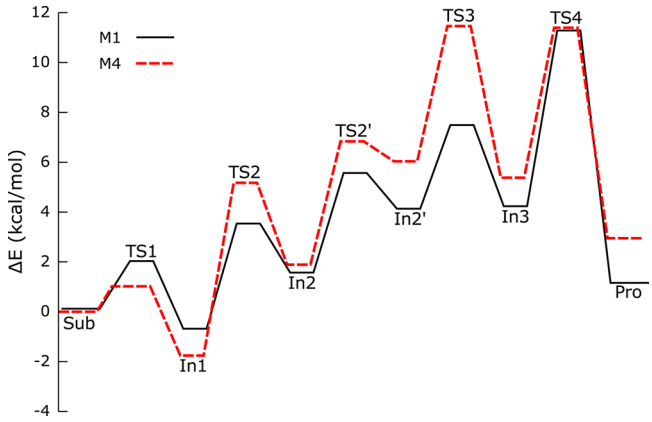

Figure 7. Reaction energy profiles (potential energy) for models M1 (black line) and M4 (red dotted line). The complete reaction path involves the substrate state (Sub), four intermediates, and the product state (Pro). In1 is the substrate-derived intermediate, which collapses into the decarboxylated intermediate In2. In2′ is similar to In2, but the conformation of the Cys503 side chain has changed. In3 is the intermediate in which Cys503 has been protonated by Glu505.

does not introduce any noticeable changes to the geometry of the model, except the new position of the carboxylic proton of Glu505, which is now bound to Cys503.

Radical-Back Transfer from the p-Hydroxybenzyl Radical to Cys503 (Step V). During the last reaction step, a hydrogen atom is transferred from the enzyme to the *p*-hydroxybenzyl radical. The optimized geometry of In3 shows that the hydrogen atom at Cys503 is 3.3 Å away from the methylene radical group (atom C7). We studied the final radical transfer by a PES scan. The distance between these two atoms was shortened in steps of −0.1 Å. The scan was followed by the NEB calculation. Mechanistically, the hydrogen atom was found to approach the methylene radical group from below the plane that is formed by the aromatic ring. Although the distance to overcome of 3.3 Å is rather long, the activation energy for this step was calculated to be only 6.1 kcal/mol (see In3→Pro in Table 2). As seen from the geometry of In3, the product-related intermediate forms only one hydrogen bond in the active site, namely with Glu637. This loose binding allows the *p*-hydroxybenzyl radical to approach Cys503 more easily in order to accept a hydrogen atom. Indeed, the NEB-calculated reaction profile shows both the Cys503 side chain and the neutral methylene radical group approach each other. Once the transition state TS4 is passed, the energy decreases by about 8.5

dx.doi.org/10.1021/ja402379q | J. Am. Chem. Soc. 2013, 135, 14574−14585

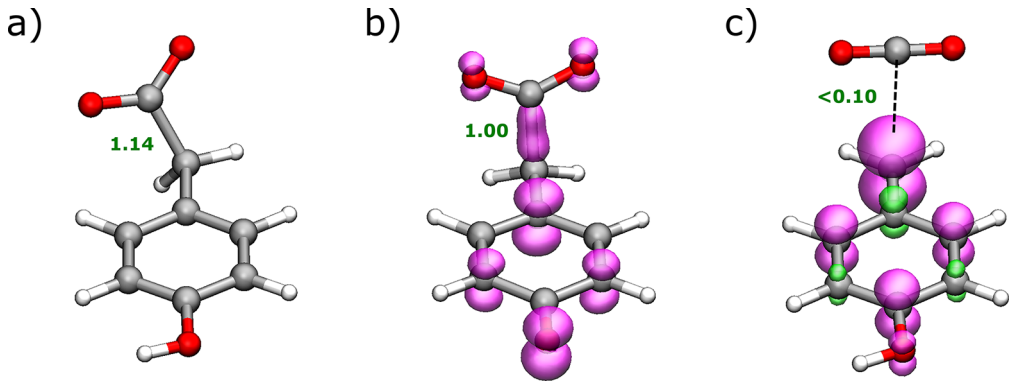

Figure 8. Optimized geometries of 4-hydroxyphenylacetate, the phenoxy-acetate radical anion and the *p*-hydroxybenzyl radical calculated using the B3LYP functional and the 6-311++G(2d,2p) basis set. The volumes show the spin density distribution. The numbers indicate the Mayer bond-order parameter between methylene carbon (C7) and the carboxyl carbon (C8). (a) 4-hydroxyphenylacetate, (b) phenoxy-acetate radical anion, (c) *p*-hydroxybenzyl radical, and carbon dioxide. As pointed out by one reviewer, the spin distribution in the phenoxy-acetate radical anion is not understandable by resonance structures often used in organic chemistry, since the methylene group at C7 impedes any resonance between the carboxyl group and the aromatic ring. In the picture of resonance structures, the spin distribution can be understood as a superposition of two radicals, one at the carboxylic group, the other at the aromatic ring. In the transition of 4-hydroxyphenylacetate to the phenoxy-acetate radical anion, the torsion angle between the aromatic ring and the carboxyl group changes from about 120° to about 90°. Interestingly, the torsion angle of 4-hydroxyphenylacetate is about 100°, i.e., close to the phenoxy-acetate radical anion. Adding a proton to the hydroxyl group of phenoxy-acetate radical anion triggers the cleavage of the bond between the methylene carbon (C7) and the carboxyl carbon (C8) and thus leads to the formation of the *p*-hydroxybenzyl radical and carbon dioxide.

kcal/mol. The resulting final product is 3.1 kcal/mol lower in energy than In3 (M4). The other models predict similar energetics. In the product state, most of the spin density is again localized at the S_γ atom of Cys503 (0.93). The remaining spin density is mainly localized on the carboxylic group of Glu505, which is now deprotonated. The optimized geometry of the final product is similar to that of In3. The two geometries differ primarily in the position of the hydrogen atom that has been transferred from Cys503 to the product. Also the distance from the methylene carbon atom (C7) of the product *p*-cresol to the carbon atom (C8) of CO_2 has increased from 2.7 to 2.9 Å.

Using the software eQuilibrator,[58] we estimate a free energy of about −4.5 kcal/mol for conversion of 4-hydroxyphenylacetate and a proton to *p*-cresol and CO_2 at pH = 7 and an ionic strength of 0.15 M (or −5.7 kcal/mol considering also the formation of carbonic acid). Thus, the overall reaction is exothermic, and our calculations suggest that a large part of the released energy is connected to the product release, since according to our calculation the product has a 2.9 kcal/mol (model M4) higher energy than the substrate inside the binding pocket. After product release, the active site has to regenerate its initial protonation state since Glu505 is deprotonated after the reaction is completed. We propose that upon binding of a new substrate molecule, Glu505 gets protonated from the solvent.

Understanding of Key Features of the Mechanism from Gas-Phase Calculations. In order to obtain a better understandable view of the reaction, we performed gas-phase calculations of the first reaction steps just considering the substrate. We tried to mimic the reactions in the enzyme. That means, first we optimized the substrate molecule 4-hydroxyphenylacetate using B3LYP and a 6-311++G(2d,2p) basis set. Next, we removed an electron from the system and a proton from the hydroxyl group. Geometry optimization by the same method lead to the phenoxy-acetate radical anion, i.e., the first intermediate. Finally, we added a proton to the hydroxyl oxygen of the optimized geometry of the phenoxy-acetate radical anion. Here geometry optimization lead to the *p*-hydroxybenzyl radical and carbon dioxide, i.e., the bond between the methylene carbon (C7) and the carboxyl carbon (C8) breaks as seen from the calculated Mayer bond orders (Figure 8). The optimized geometries are depicted in Figure 8. Hence after these reaction, carbon dioxide is free to leave. The remaining reaction is the addition of a hydrogen atom to *p*-hydroxybenzyl radical from Cys503 in order to form *p*-cresol. These results on the reactions in the gas phase corroborate our mechanism and indicate that the protonation of the phenolic hydroxyl group facilitates the release of carbon dioxide from the phenoxy-acetate radical anion.

The optimal torsion angle of the carboxyl group (torsion C2−C1−C7−C8) in 4-hydroxyphenylacetate is about 120° (see Figure 8a). This torsion angle changes to about 90° in the phenoxy-acetate radical anion (Figure 8b). Interestingly, this angle is about 100° in the crystal structure, i.e., closer to the value in the phenoxy-acetate radical anion. Thus, 4Hpad stabilizes the first intermediate, as one would expect from an efficient enzyme.

■ CONCLUSIONS

We have employed continuum electrostatic and QC/MM calculations to study the catalytic mechanism of 4-hydroxyphenylacetate decarboxylase, a novel glycyl radical enzyme. The calculations suggest an unusual activation mode of the substrate that involves two simultaneous transfers which are separated in space, an electron transfer from the substrate to Cys503 and the proton transfer from the phenolic group of the substrate to Glu637. Thus, the substrate is activated by the abstraction of an electron and a proton, i.e., *de facto* a hydrogen atom, which is a common starting point in radical enzyme catalysis.[5] However, that the electron and the proton are transferred to different groups of the active site is to our knowledge unprecedented. The loss of the electron from the substrate weakens the C−C bond of its acetate moiety. The decarboxylation is coupled to a proton transfer from Glu637 back to the phenolic hydroxyl group. The final steps of the

dx.doi.org/10.1021/ja402379q | J. Am. Chem. Soc. 2013, 135, 14574−14585

reaction involve rotation of the Cys503 side chain and a proton transfer from Glu505 to Cys503. The reaction is completed by a hydrogen atom transfer from Cys503 to the *p*-hydroxybenzyl radical yielding the product *p*-cresol. The energetics calculated for each reaction step are all very plausible with the highest energy barrier of 6.1 kcal/mol for the last reaction step. The complete reaction profile for models M1 and M4 is summarized in Figure 7.

On the basis of our calculations, we propose the following roles for active site residues in the catalysis. Cys503 is a radical relay that accepts an electron from the substrate and later in the reaction donates a hydrogen atom, as postulated for glycyl radical enzymes.[5] Glu637, which is hydrogen bonded to the hydroxyl group of the substrate, is a proton acceptor/donator involved in substrate activation and decarboxylation. The pair of residues Cys503 and Glu637 seems to be crucial for catalysis. The second glutamate in the active site, Glu505, starts in the reaction cycle in a protonated form and later donates the proton to Cys503. Prior to the activation step, Glu505 forms a hydrogen bond to the carboxylic group of the substrate. Ser344 provides another hydrogen bond on the opposite side of this group. Thus, Glu505 and Ser344 seem to play a role in substrate binding. The electrostatic calculations predict that His536 is positively charged. This positive charge helps stabilize both the negatively charged Glu637 in the substrate-bound state and the negatively charged first intermediate state.

Our calculations agree with experiments which indicate that the hydroxyl group in the *para*-position of the substrate is essential for the catalysis by 4Hpad. Ligands lacking a hydroxyl group in this position have been reported as competitive inhibitors of the enzyme.[12] This observation can now be explained on the basis of the calculated activation mode of the ligand. Namely, Glu637, which is hydrogen bonded to this hydroxyl group, does not only play a role in ligand binding but is also important for the catalysis as a proton acceptor/donator.

From the computational perspective, the QC/MM models used in this paper that differ in the size of the QC part give similar energetics and nearly the same geometries of the minima. If a smaller basis set is used for the QC part, the discrepancies in barrier prediction between the models usually do not exceed 1.0 kcal/mol. The use of a larger basis set can further reduce these discrepancies (see Table 2). Somewhat larger differences can only be observed in step I. All models studied herein consistently predict the same reaction mechanism. We are therefore confident that we provide a realistic explanation for the unprecedented Kolbe-type decarboxylation catalyzed by 4-hydroxyphenylacetate decarboxylase.

■ ASSOCIATED CONTENT

Supporting Information

Cartesian coordinates and Mulliken atomic spin populations and charges for the optimized structures; titration curves of active site residues; NEB-derived reaction profiles for models M1−M3; discussion of the unlikeness of an alternative mechanism, which was proposed before the structure was determined; and an animation showing the complete NEB-derived reaction path for model M4. This material is available free of charge via the Internet at http://pubs.acs.org.

■ AUTHOR INFORMATION

Corresponding Author

Matthias.Ullmann@uni-bayreuth.de

Notes

The authors declare no competing financial interest.

■ ACKNOWLEDGMENTS

This work was supported by the DFG grants UL 174/8-2 and MA 3348/2-1 as well as by the BioMedTec International Graduate School of the Elitenetwork Bavaria.

■ REFERENCES

(1) Buckel, W.; Golding, B. *FEMS Microbiol. Rev.* **1998**, *22*, 523−541.
(2) Stubbe, J.; van der Donk, W. A. *Chem. Rev.* **1998**, *98*, 705−76.
(3) Eklund, H.; Fontecave, M. *Struct. Fold. Des.* **1999**, *7*, R257−R262.
(4) Frey, P. *Annu. Rev. Biochem.* **2001**, *70*, 121−148.
(5) Frey, P. A.; Hegeman, A. D.; Reed, G. H. *Chem. Rev.* **2006**, *106*, 3302−3316.
(6) Buckel, W.; Golding, B. T. *Annu. Rev. Microbiol.* **2006**, *60*, 27−49.
(7) Buckel, W. *Angew. Chem., Int. Ed.* **2009**, *48*, 6779−6787.
(8) Buckel, W.; Zhang, J.; Friedrich, P.; Parthasarathy, A.; Li, H.; Djurdjevic, I.; Dobbek, H.; Martins, B. M. *Biochem. Biophys. Acta* **2012**, *1824*, 1278−1290.
(9) Selmer, T.; Pierik, A.; Heider, J. *Biol. Chem.* **2005**, *386*, 981−988.
(10) Frey, P. A.; Hegeman, A. D.; Ruzicka, F. J. *Crit. Rev. Biochem. Mol. Biol.* **2008**, *43*, 63−88.
(11) Craciun, S.; Balskus, E. P. *Proc. Natl. Acad. Sci. U.S.A.* **2012**, *109*, 2130721312.
(12) Selmer, T.; Andrei, P. *Eur. J. Biochem.* **2001**, *268*, 1363−1372.
(13) Andrei, P.; Pierik, A.; Zauner, S.; Andrei-Selmer, L.; Selmer, T. *Eur. J. Biochem.* **2004**, *271*, 2225−2230.
(14) Yu, L.; Blaser, M.; Andrei, P. I.; Pierik, A. J.; Selmer, T. *Biochemistry* **2006**, *45*, 9584−9592.
(15) Dari, L.; Barker, H. *Arch. Microbiol.* **1985**, *143*, 311−312.
(16) Dawson, L. F.; Stabler, R. A.; Wren, B. W. *J. Med. Microbiol.* **2008**, *57*, 745−749.
(17) Martins, B. M.; Blaser, M.; Feliks, M.; Ullmann, G. M.; Buckel, W.; Selmer, T. *J. Am. Chem. Soc.* **2011**, *133*, 14666−14674.
(18) Vijh, A.; Conway, B. *Chem. Rev.* **1967**, *67*, 623−664.
(19) Himo, F.; Siegbahn, P. *Chem. Rev.* **2003**, *103*, 2421−2456.
(20) Lee, J.; Houk, K. *Science* **1997**, *276*, 942−945.
(21) Lee, T.; Chong, L.; Chodera, J.; Kollman, P. *J. Am. Chem. Soc.* **2001**, *123*, 12837−12848.
(22) Lundberg, M.; Blomberg, M.; Siegbahn, P. *J. Mol. Model.* **2002**, *8*, 119−130.
(23) Wang, J.; Dong, H.; Li, S.; He, H. *J. Phys. Chem. B* **2005**, *109*, 18664−18672.
(24) Silva, P.; Ramos, M. *J. Phys. Chem. B* **2005**, *109*, 18195−18200.
(25) Silva, P. J.; Ramos, M. J. *J. Phys. Chem. B* **2007**, *111*, 12883−12887.
(26) Moya-Garcia, A. A.; Ruiz-Pernia, J.; Marti, S.; Sanchez-Jimenez, F.; Tunon, I. *J. Biol. Chem.* **2008**, *283*, 12393−12401.
(27) Himo, F.; Eriksson, L. *J. Am. Chem. Soc.* **1998**, *120*, 11449−11455.
(28) Lucas, M.; Fernandes, P.; Eriksson, L.; Ramos, M. *J. Phys. Chem. B* **2003**, *107*, 5751−5757.
(29) Guo, J.; Himo, F. *J. Phys. Chem. B* **2004**, *108*, 15347−15354.
(30) Condic-Jurkic, K.; Perchyonok, V. T.; Zipse, H.; Smith, D. M. *J. Comput. Chem.* **2008**, *29*, 2425−2433.
(31) Condic-Jurkic, K.; Zipse, H.; Smith, D. M. *J. Comput. Chem.* **2010**, *31*, 1024−1035.
(32) Himo, F. *J. Phys. Chem. B* **2002**, *106*, 7688−7692.
(33) Himo, F. *Biochim. Biophys. Acta* **2005**, *1707*, 24−33.
(34) Himo, F. *Chem. Phys. Lett.* **2000**, *328*, 270−276.
(35) Hioe, J.; Savasci, G.; Brand, H.; Zipse, H. *Chem.—Eur. J.* **2011**, *17*, 3781−3789.
(36) Liu, Y.; Gallo, A. A.; Florian, J.; Liu, Y.-S.; Mora, S.; Xu, W. *J. Phys. Chem. B* **2010**, *114*, 5497−5502.
(37) Liu, Y.; Gallo, A. A.; Xu, W.; Bajpai, R.; Florian, J. *J. Phys. Chem. A* **2011**, *115*, 11162−11166.

(38) Feliks, M.; Ullmann, G. M. *J. Phys. Chem. B* **2012**, *116*, 7076−7087.
(39) Bashford, D.; Karplus, M. *J. Phys. Chem.* **1991**, *95*, 9556−9561.
(40) Ullmann, G. M.; Knapp, E. W. *Eur. Biophys. J.* **1999**, *28*, 533−551.
(41) Bombarda, E.; Ullmann, G. M. *J. Phys. Chem. B* **2010**, *114*, 1994−2003.
(42) Field, M. *J. Comput. Chem.* **2002**, *23*, 48−58.
(43) Senn, H. M.; Thiel, W. *Angew. Chem.-Int. Edit.* **2009**, *48*, 1198−1229.
(44) Galvan, I. F.; Field, M. J. *J. Comput. Chem.* **2008**, *29*, 139−143.
(45) Aleksandrov, A.; Field, M. *Phys. Chem. Chem. Phys.* **2012**, *14*, 12544−12553.
(46) Brooks, B. R.; Bruccoleri, R. E.; Olafson, B. D.; States, D. J.; Swaminathan, S.; Karplus, M. *J. Comput. Chem.* **1983**, *4*, 187−217.
(47) Brooks, B. R.; Brooks, C. L., III; Mackerell, A. D., Jr.; Nilsson, L.; Petrella, R. J.; Roux, B.; Won, Y.; Archontis, G.; Bartels, C.; Boresch, S.; Caflisch, A.; Caves, L.; Cui, Q.; Dinner, A. R.; Feig, M.; Fischer, S.; Gao, J.; Hodoscek, M.; Im, W.; Kuczera, K.; Lazaridis, T.; Ma, J.; Ovchinnikov, V.; Paci, E.; Pastor, R. W.; Post, C. B.; Pu, J. Z.; Schaefer, M.; Tidor, B.; Venable, R. M.; Woodcock, H. L.; Wu, X.; Yang, W.; York, D. M.; Karplus, M. *J. Comput. Chem.* **2009**, *30*, 1545−1614.
(48) MacKerell, A. D.; et al. *J. Phys. Chem. B* **1998**, *102*, 3586−3616.
(49) Torres, R.; Lovell, T.; Noodleman, L.; Case, D. *J. Am. Chem. Soc.* **2003**, *125*, 1923−1936.
(50) Bashford, D.; Gerwert, K. *J. Mol. Biol.* **1992**, *224*, 473−486.
(51) Ullmann, R. T.; Ullmann, G. M. *J. Comput. Chem.* **2012**, *33*, 887−900.
(52) Field, M. J. *J. Chem. Theory Comput.* **2008**, *4*, 1151−1161.
(53) Neese, F. *Wiley Interdiscip. Rev.: Comput. Mol. Sci.* **2012**, *2*, 73−78.
(54) Vosko, S.; Wilk, L.; Nusair, M. *Can. J. Phys.* **1980**, *58*, 1200−1211.
(55) Lee, C.; Yang, W.; Parr, R. *Phys. Rev. B* **1988**, *37*, 785−789.
(56) Becke, A. *J. Chem. Phys.* **1993**, *98*, 5648−5652.
(57) Stephens, P.; Devlin, F.; Chabalowski, C.; Frisch, M. *J. Phys. Chem.* **1994**, *98*, 11623−11627.
(58) Flamholz, A.; Noor, E.; Bar-Even, A.; Milo, R. *Nucleic Acids Res.* **2012**, *40*, D770−D775.
(59) Humphrey, W.; Dalke, A.; Schulten, K. *J. Mol. Graphics* **1996**, *14*, 33−38.